Construction and test of a 1x1 m^2 Micromegas chamber for sampling hadron calorimetry at future lepton colliders

C. Adloff[a], J-J. Blaising[a], M. Chefdeville[a*], A. Dalmaz[a], C. Drancourt[a], R. Gaglione[a], N. Geffroy[a], D. Girard[a], J. Jacquemier[a], Y. Karyotakis[a], I. Koletsou[a], F. Peltier[a], J. Samarati[a], S. Tsigaridas[b], G. Tsipolitis[b] and G. Vouters[a]

[a] *Laboratoire d'Annecy-le-Vieux de Physique des Particules, Université de Savoie, CNRS/IN2P3*
9 Chemin de Bellevue - BP 110, 74941 Annecy-le-Vieux Cedex, France
[b] *NTUA, National Technical University of Athens,*
Zografou Campus, GR-157, 80 Zografou, Greece
E-mail: chefdevi@lapp.in2p3.fr

ABSTRACT: Gaseous sampling hadron calorimeters can be finely segmented and used to record showers with high spatial resolution. This imaging power can be exploited at a future linear collider experiment where the measurement of jet energy by a Particle Flow method will rely first on the tracking capability of the calorimeters. Gaseous detectors can easily achieve any desired granularity and a hadron sampling calorimeter using gas as sensitive material and simple threshold electronics is considered. For this application, Micromegas chambers of a few meter square size offer some advantages over traditional gaseous detectors using wires or resistive plates. To test the validity of this concept, a Micromegas prototype of $1 \times 1\,\mathrm{m}^2$ size equipped with 9216 readout pads of $1 \times 1\,\mathrm{cm}^2$ has been built. Its technical and basic operational characteristics are reported.

KEYWORDS: Keyword1; Keyword2; Keyword3.

*Corresponding author.

Contents

1. Introduction **2**
1.1 Particle Flow calorimetry 2
1.2 Semi-digital hadron calorimetry 2
1.3 The Micromegas detector and calorimeter project 2

2. Description of the $1 \times 1\,\mathrm{m}^2$ Micromegas prototype **3**
2.1 Active sensor units 3
2.2 Front-end electronics 3
2.3 Mechanical design 4

3. Tests prior to chamber assembly **4**
3.1 Electronics calibration 4
3.1.1 Method 4
3.1.2 Shaper gains and noise 5
3.1.3 Setting of thresholds and pedestals 6
3.2 X-ray tests 6
3.2.1 Threshold scans 7
3.2.2 Mesh voltage scan 8
3.2.3 Position scan 9

4. Functional tests of the prototype in particle beams **10**
4.1 Noise conditions in triggered operation 11
4.2 Trigger-less operation 11
4.3 Response of the six Micromegas meshes 12
4.4 Effect of the peaking time 13
4.5 Impact of dead zones between ASUs 14
4.6 Shower sampling with three readout thresholds 16
4.7 Analogue readout of shaper signals 16
4.8 Power-pulsing of the front-end chips 17

5. Conclusion **17**

1. Introduction

1.1 Particle Flow calorimetry

The detailed study of electroweak symmetry breaking and of the properties of the Higgs boson are some of the physics goals motivating the construction of a linear electron collider (ILC [1] or CLIC [2]). This physics case is now enhanced with the discovery at LHC of a Higgs-like new particle [3, 4]. Most of the interesting physics channels at a linear collider will appear in multi-jet final states, often accompanied by charged leptons and missing transverse energy. The dijet mass resolution should be good enough to identify Z and W bosons in their hadronic decay channels with an accuracy comparable to their natural decay width. This requires an excellent jet energy resolution of 3–4 % over the whole energy range.

Two techniques are studied by the DREAM [5] and CALICE [6] collaborations to meet this goal. The first one, called Dual Readout, is a compensation technique that uses cherenkov and scintillation light produced in hadron showers to correct for fluctuations of the electromagnetic fraction which otherwise dominate the jet energy resolution [7]. The Particle Flow technique uses highly segmented calorimeters and a precise tracker to separate the jet's charged and neutrals components [8]. After separation, the dominant charged component can be measured more precisely with the tracking system resulting in improved jet energy resolution [9].

1.2 Semi-digital hadron calorimetry

Two hadron calorimeters using steel or tungsten absorbers are developed by the the CALICE collaboration. The first is instrumented with $3 \times 3\,\mathrm{cm}^2$ scintillating tiles read out by SiPM and 12-bit ADCs [10]. The second uses gaseous detectors with smaller segmentation ($1 \times 1\,\mathrm{cm}^2$) and simpler readout (1-bit or 2-bit [11, 12]). Clearly, the first favours single hadron resolution (higher sampling fraction, analogue readout) while the second targets a high shower separation capability (smaller cells) probably at the expense of resolution (digital readout).

A digital hadron calorimeter (1-bit, DHCAL) is expected to have two regimes of operation. A low energy linear regime where the response to the electromagnetic and hadronic shower parts, taken separately, is constant. In this regime, Landau fluctuations are suppressed resulting in improved resolution with respect to a perfect analogue readout. A higher energy saturated regime where the energy information is lost due to under-counting with the consequence that the resolution degrades with increasing hadron energy [13, 14]. The energy frontier between the two regimes depends mainly on the cell size and absorber material. In an SiD-like HCAL geometry with $1 \times 1\,\mathrm{cm}^2$ pads and steel absorbers [15], Monte Carlo simulation indicates a frontier between 20–30 GeV.

The electromagnetic part of hadron showers results in dense energy deposits and is responsible for the saturation of a DHCAL. A way to account for these deposits in the energy reconstruction is to use additional readout thresholds (2-bit, semi-digital HCAL or SDHCAL). With the right threshold settings and energy reconstruction algorithm, it should be possible to correct for the saturation and improve to some extend the resolution.

1.3 The Micromegas detector and calorimeter project

Micromegas is a Micro Pattern Gas Detector (MPGD) that uses a thin mesh to separate the gas

volume into two regions [16]. A low field region where primary electrons are released from the atoms and a high field region where they are drifted to and multiplied by avalanche. Thanks to a fast collection of the avalanche ions, Micromegas is free of space charge effects up to very high particle rates and therefore well suited for tracking in high rate environments. This property also makes this detector very appealing for calorimetry because signals are proportional to the energy deposited in the drift region. This is an improvement with respect to wire chamber based gaseous calorimeters which suffered from intrinsic signal saturation from the ion space charge around the wire. Also, ageing effects in Micromegas are minimal because it works in simple gas mixtures (*e.g.* Ar/CO_2) and at relatively low electric fields ($\sim 40\,kV/cm$ with a multiplication gap of $128\,\mu m$).

The Micromegas calorimeter project was initiated in 2006. The first step of the project was the characterisation of small prototypes equipped with standard electronics (external front-end boards and VME ADC modules). Based on the successful results [17], the project moved on to the next phase, namely the integration of the electronics on the detector printed circuit board (PCB) and the scaling up of the detector size.

2. Description of the $1 \times 1\,m^2$ Micromegas prototype

2.1 Active sensor units

An Active Sensor Unit (or ASU) is a $32 \times 48\,cm^2$ PCB (8 layers, 1.2 mm thin) segmented into 1536 anode pads of $1 \times 1\,cm^2$. It is equipped with a Micromegas mesh and 24 front-end chips. The mesh is laminated on the PCB pad plane according to the Bulk process [18]. Packaged chips are soldered to the PCB side opposite to the mesh, together with spark protection diodes, other passive components and flat connectors.

The ASU chips are read out with 2 Detector Interface boards (DIF, inter-DIF) which also distribute voltage to the front-end electronics and to the Micromegas mesh. ASU and inter-DIF are connected with flat cables in order to minimise the detector thickness and to allow for some mechanical flexibility between the 2 boards. Thanks to flat connectors on both sides of the ASU, several ASUs can be read out in a row (Figure 1 (left)). This is essential in view of the construction of large area chambers as several ASUs can be chained and read out with only one pair of DIF/inter-DIF boards.

2.2 Front-end electronics

The ILC beam will be pulsed and composed of 1 ms long bunch trains separated by 199 ms. During a train, bunches cross each other every 300 ns and calorimeter signals are digitised automatically and associated to the time of a bunch. Between trains, all information is read out from memory to the back-end electronics meanwhile some front-end circuits are turned off to reduce the heat dissipation inside the calorimeter modules. Key features of the front-end electronics are thus self-triggering with memory, time-stamping and power-pulsing.

A dedicated front-end chip called MICROROC has been developed [19]. It belongs to a generation of chips optimised for calorimetry at a future linear collider [20]. The MICROROC is a 64 channel chip, with 3 readout thresholds and a power-pulsing capability to reduce its consumption from a nominal value of 3.7 mW at 3.5 V per channel to $100\,\mu W$. Each channel input is protected

against spark currents by a diode network followed by a charge preamplifier and 2 shapers of low/high gains and tunable peaking time (75–200 ns). The shaper outputs are connected to three discriminators. When a signal crosses the low threshold, the content of the 64 channel matrix is written to memory with a clock time (so-called event). A total of 127 events can be recorded before filling completely the memory. The later is read out either when it is full (ILC or trigger-less mode) or upon the arrival at the chip of an external trigger signal (testbeam mode or trigger mode).

The high gain shaper is connected to the low and medium threshold discriminators and has a dynamic range of 200 fC. The low gain shaper has a linear response up to 500 fC and is connected to the high threshold discriminator. The 3 thresholds are set by 10-bit DACs common to the 64 channels. Per channel a 4-bit DAC can be used to shift the pedestal voltage with respect to the common thresholds and minimise their dispersions. A detailed characterisation of the detector can be performed thanks to the calibration test input and a multiplexed shaper output (analogue readout). Calibration of the electronics is discussed in section 3.1 and the analogue readout of Micromegas signals is explained in section 4.7.

2.3 Mechanical design

Mechanical constraints to build an ILC hadron calorimeter are stringent. First of all, the calorimeter will be located inside the solenoid magnet which limits its total depth to preserve cost; the envisaged space space between absorbers is 8 mm. Also, to minimise dead zones between modules, the font-end electronics is embedded inside the active layers and only readout boards are foreseen at the ends of the modules. Another challenge is the size of active layers which reaches up to $1 \times 3\,\mathrm{m}^2$ in the SiD design.

Modular and scalable to larger sizes, the $1 \times 1\,\mathrm{m}^2$ Micromegas prototype consists of 6 ASUs assembled in a one gas volume (Figure 1). Small spacers are inserted in the 1 mm gap between ASUs and support the cathode cover, defining precisely a drift gap of 3 mm (Figure 2). Plastic frames are closing the chamber sides, leaving openings for 2 gas pipes and flat cables for electronics connections. The chamber is eventually equipped with readout boards (3 pairs of DIF/inter-DIF) and a patch panel for voltage distribution.

The total chamber thickness amounts to roughly 9 mm which includes 2 mm for the cathode cover, 3 mm of drift gap and less than 4 mm for PCB and ASICs. With this mechanical design, the fraction of non-instrumented area is less than 2 % of the total area defined by the 6 ASUs. Dead zones are mainly caused by the 1 mm gap between ASUs and the 2 mm wide inactive photoresist strips that support the mesh on the four ASU sides.

3. Tests prior to chamber assembly

3.1 Electronics calibration

3.1.1 Method

The calibration enables setting the 3 thresholds by providing the electronic gain (DAC/fC) of the two shapers. It consists in injecting voltage pulses to the test capacitor of each channel and changing the relevant threshold every 100 pulses. For a given pulse height (or test charge), the channel response (0/1) versus threshold is measured and latter differentiated. The gain and noise of the

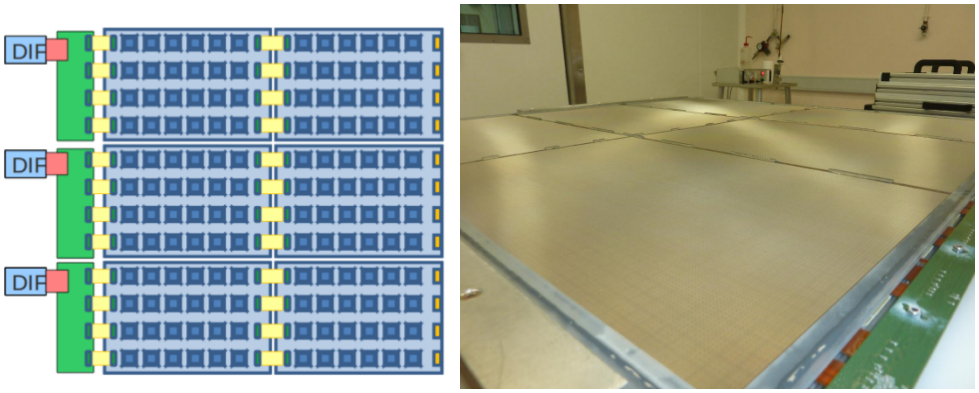

Figure 1. Drawing of the chip side of the $1 \times 1\,m^2$ prototype showing the readout boards (DIF, inter-DIF), the ASUs and the flexible connectors between them (left). Photograph of the mesh side of the prototype and the drift cover during assembly (right).

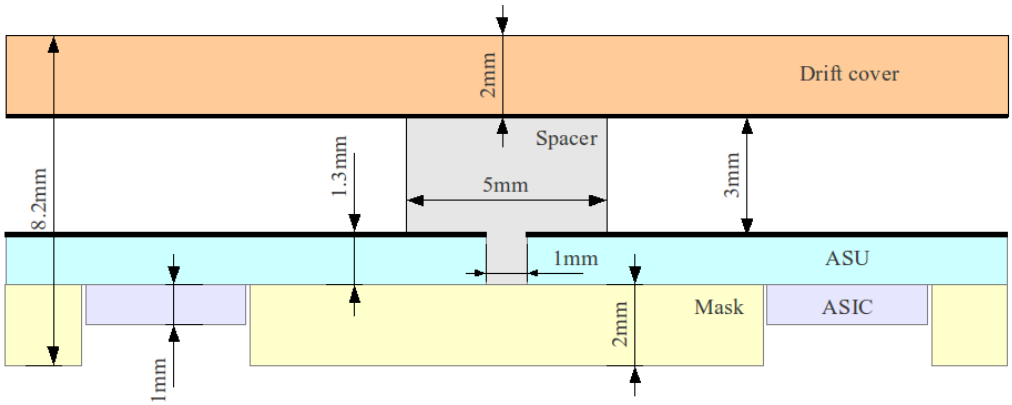

Figure 2. Mechanical design of the $1 \times 1\,m^2$ prototype at a junction between 2 ASU.

shapers is deduced from the mean μ and root mean squared (RMS) σ of the resulting distribution. Non-linearity of the shaper response is also checked by injecting different test charges: 2.5, 12.5, 22.5 and 32.5 fC for the high gain shaper and 100 and 200 fC for the low gain shaper. The electronic calibration was performed with a single chip test board after the MICROROC production. According to the rejection criteria defined in [19], a yield of 91.5 % was found. After bounding of the chips to the PCBs and lamination of the Bulk mesh, another calibration was performed on the 6 available ASU giving compatible results. These results are presented in the following section.

3.1.2 Shaper gains and noise

The gain of the shapers of 9216 channels is distributed around a mean value of 7.0 DAC/fC (high gain) and 1.6 DAC/fC (low gain). The channel to channel variation in both cases is ~ 3 % RMS (Figure 3 (left and centre)). This is 3 times smaller than the signal variations induced by mechanical imperfections of the Micromegas gaps which eventually dominate the response uniformity of this Micromegas detector [17].

The low threshold discriminator triggers the writing to memory of the 64 channel content. It

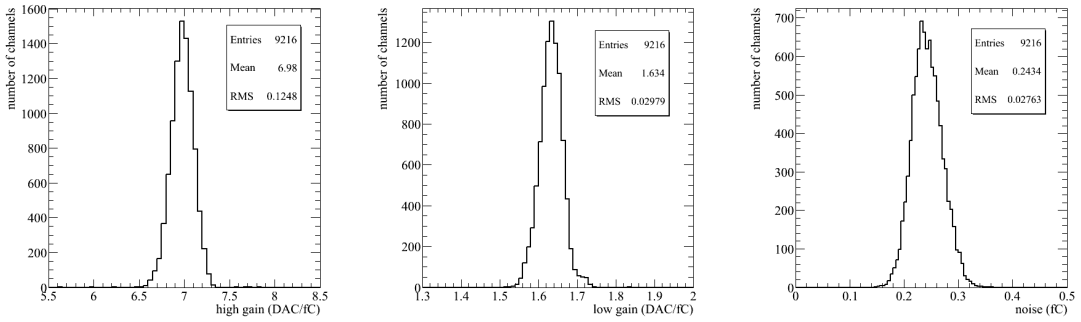

Figure 3. From left to right: gains of the 2 shapers and noise at the output of the high gain shaper for all channels of the $1 \times 1\,\mathrm{m}^2$ prototype.

is connected to the output of the high gain shaper and therefore only the noise of this shaper is relevant for our purposes. Calculating the noise as σ divided per the gain, an average noise of 0.25 fC is found with variations of 10 % RMS over all channels. This is quite small compared to a typical Micromegas MIP signal of 5–10 fC and close to what was measured before bounding of the chips to the PCB. It can thus be concluded that neither the design of the PCB nor the lamination of the mesh increase the noise level at the channel inputs.

3.1.3 Setting of thresholds and pedestals

The 3 discriminator DACs of a MICROROC are common to the 64 channels. The lowest possible threshold is therefore determined by the channel with the highest pedestal, for instance 5 σ above this pedestal. Also, channels with lower pedestals will experience larger thresholds. As a result, each channel was also equipped with a pedestal DAC. The latter controls the pedestal voltage and can be used to correct the individual thresholds by a few fC. A method to align the pedestals (and thus to equalise the thresholds) is to set the pedestal DACs such as to obtain a uniform noise rate over all the channels. With this method, the spread of thresholds is reduced by a factor of 2 as illustrated in Figure 4. This is of significant value because a smaller threshold spread allows a lower operating gas gain and low gain operation is always preferred.

In a semi-digital calorimeter, values of the medium and high thresholds should be optimised for best energy resolution over the relevant energy range. During the test beam period reported in section 4, default settings of 5 and 15 MIPs have been chosen.

3.2 X-ray tests

Counting experiments are performed with an ^{55}Fe 5.9 keV X-ray source to characterise the ASUs before they are sealed in the $1 \times 1\,\mathrm{m}^2$ prototype. A dedicated gaseous chamber with 14 mm drift gap and perforated drift cover has been constructed to measure the response of any of the 1536 ASU channels to true Micromegas signals.

In a non flammable mixture of Ar/CF_4/$i C_4H_{10}$ 95/3/2, ^{55}Fe quanta can convert in the gas mainly by photoelectric effect on an argon atom, resulting on average in 115 or 230 primary electrons depending on the involved atom relaxation process: fluorescence (escape peak) or Auger

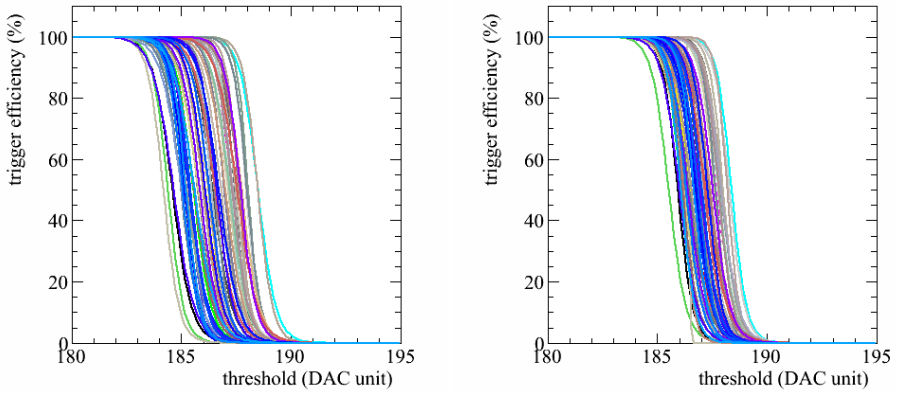

Figure 4. Pedestals of 64 channels measured in a threshold scan before and after alignment (left and right).

cascade (photopeak) [21]. After drifting, mostly all primary electrons are multiplied in the amplification gap [17]. If above threshold, the pad signal is recorded as a hit in the chip memory. The counting rate was measured for various sets of experimental parameters (thresholds, mesh voltage and pad position). Each run lasted 60 s and the drift field was set to 300 V/cm which corresponds to the local maximum of the drift velocity in the gas mixture used. Results are presented and discussed in the following sections.

3.2.1 Threshold scans

The gas gain curve is deduced from measurements of the counting rate R versus threshold t at various mesh voltages and using inputs from the electronic calibration (shaper gains). Low threshold scans were performed at voltages between 300 and 350 V. At a drift field of 300 V/cm, the average spread of a point-like cloud of electrons (from photoelectric conversion) at the mesh is $\sim 230\,\mu$m in the direction transverse to the field and ~ 2 ns in time [22]. With the source collimated to the centre of a pad, most primary electrons are collected on one pad. For simplicity all other pads were electronically disabled. The results are shown in Figure 5. Each $R(t)$ trend is well described by the sum of two sigmoid functions accounting for the photopeak and the escape peak:

$$R(t) = \frac{p_0}{1+\exp\left(\frac{t-p_1}{p_2}\right)} + \frac{p_3}{1+\exp\left(\frac{t-p_4}{p_5}\right)} \tag{3.1}$$

where the parameters (p_0, p_3) are the rates at zero threshold, (p_1, p_4) the inflexion thresholds at the peak maxima and (p_2, p_5) are proportional to the peak widths. In order to reduce the number of parameters fitted to the data points, the following approximations between photopeak and escape peak are used:

$$\frac{p_0}{p_3} = \frac{1-f}{f} = \frac{85}{15} \tag{3.2}$$

where f is the fluorescence yield of an excited argon atom [23]. Noting E_{pp} and E_{ep} the energy of the photopeak and escape peak:

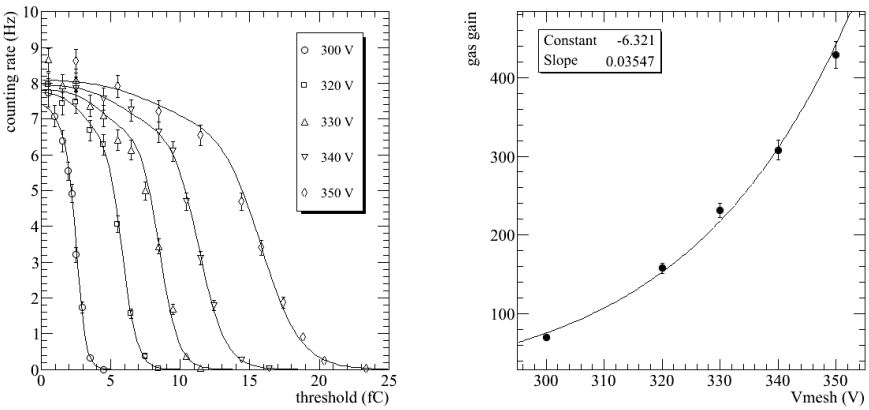

Figure 5. Counting rate versus threshold (left) and resulting gas gain curve (right).

$$\frac{p_1}{p_3} = \frac{E_{\text{pp}}}{E_{ep}} = 2 \tag{3.3}$$

$$\frac{p_2}{p_3} = \sqrt{\frac{E_{\text{pp}}}{E_{ep}}} = \sqrt{2} \tag{3.4}$$

so Equation 3.1 becomes:

$$R(t) = p_0 \left[\frac{0.85}{1+\exp\left(\frac{t-p_1}{p_2}\right)} + \frac{0.15}{1+\exp\left(\frac{t-0.5p_1}{p_2/\sqrt{2}}\right)} \right] \tag{3.5}$$

After fitting, all hit rates converge to roughly 8 Hz at zero threshold. Taking an average of 230 primary electrons for photopeak events, the measured charge at the inflexion points (p_1) is used to calculate the gas gain. The gain exhibits the usual exponential dependence on the mesh voltage (Figure 5) with a slope of 0.032 / V typical of argon-based gas mixtures [24]. At 350 V, a scan of the high threshold was performed too. The resulting $R(t)$ trend is showed in Figure 6 together with the low threshold trend. The two threshold scans give gas gain values of 323 and 300 respectively. The agreement is reasonable and the 4 % difference can probably be explained by systematic errors during the calibration.

3.2.2 Mesh voltage scan

The smallest detectable charge can be deduced from a measurement of the counting rate versus gas gain. In this study, the source is still collimated to the centre of a single pad while the other pads are disabled. The threshold of the tested pad is set by iteratively decreasing the discriminator DAC until the count rate becomes dominated by noise. The final DAC value is then set one unit above this steep transition so this configuration can be defined as the configuration of lowest workable threshold.

The counting rate is measured at various mesh voltages (200–400 V) in this configuration of lowest threshold. As showed in Figure 6 (right), it increases with voltage as the charge spectrum

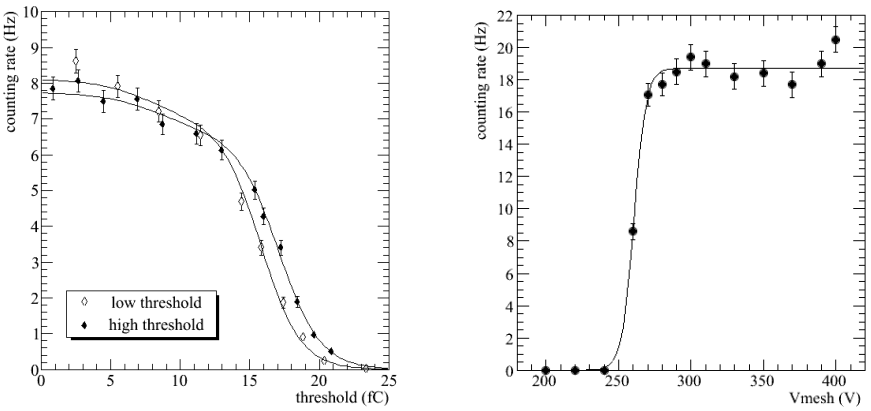

Figure 6. Counting rate versus threshold (left) and mesh voltage (right).

shifts above threshold. The trend can be described by an sigmoid function with an inflexion point at 260 V. At this voltage, the rate is by definition half of its maximum value which implies that the threshold is equal to the average pad charge. The smallest detectable charge is then given by:

$$Q = q_e \, N \, G = 1.6 \cdot 10^{-4} \cdot 212 \cdot 20 \approx 0.7\,\text{fC} \tag{3.6}$$

where N is averaged over the ^{55}Fe spectrum (*i.e.* $0.85 \cdot 230 + 0.15 \cdot 115$). Previous measurements showed that high MIP efficiency (>95 %) is reached when the most probable value of the charge is ~ 3 times larger than the threshold [17]. Taking a most probable number of primary electrons of 14 (ref X), it can be inferred this condition will be met at gas gains of 1000–2000 only.

3.2.3 Position scan

The uniformity of the gas gain and of the thresholds can be verified by measuring the X-ray counting rate at various positions and for different ASUs. For a given ASU, the position scan is performed on 6 different positions. At each position the source is collimated onto a region of 2×2 pads centred in between 4 chips (Figure 7 (left). In this way, it is possible to involve all 24 ASU chips in the counting experiment. For this study, all channels are enabled and their thresholds are equalised according to the procedure explained in section 3.1.3. The mesh voltage is set at 320 V at which an average ^{55}Fe signal of ~ 5 fC is expected. Given the collimation of the source and the transverse electron diffusion in the gas, the count rate is now to be calculated over an 8×8 pad region.

Position scans have been performed for 6 ASU before assembly in the $1 \times 1\,\text{m}^2$ prototype. As illustrated in Figure 7 (right), the response of the channels to the source is uniform. A flat noise-free background from cosmic particles can be seen when plotting the channel occupancy in a logarithmic scale. The results are summarised in Table 1. For each ASU, the spread of the counting rate was observed not to exceed 3 % RMS. Small ASU to ASU variations of the mean rate are observed, probably due to change of atmospheric conditions from one test to the next.

The conclusion of the ASU tests prior assembly inside the $1 \times 1\,\text{m}^2$ prototype is that the manufacturing technique and the calibration procedure allow to achieve very low detection threshold,

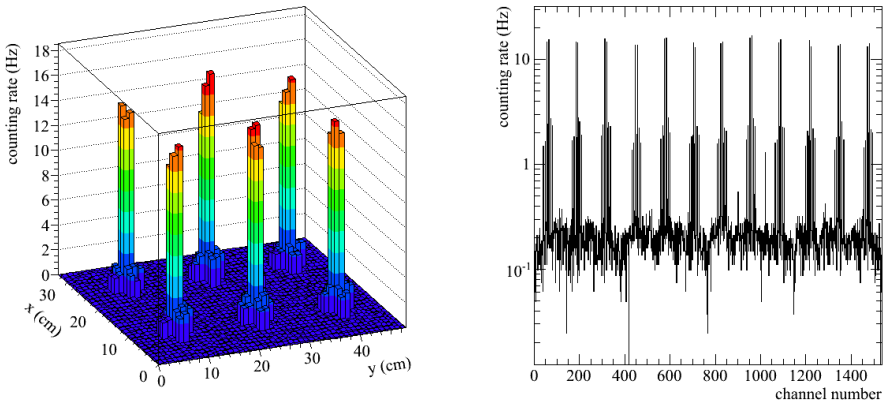

Figure 7. From left to right: two dimensional and one dimensional channel occupancy obtained when moving an ^{55}Fe source over 6 positions.

ASU number	1	2	3	4	5	6
Mean rate (Hz)	86	85	87	79	84	84

Table 1. *^{55}Fe quanta counting rates ($\pm$ 3 Hz error) measured on 6 ASU (6 measurements per ASU).*

negligible noise and good response uniformity in a reproducible way. After careful characterisation of 6 ASU, the first $1 \times 1\,\mathrm{m}^2$ Micromegas prototype with MICROROC readout was constructed in May 2011 and subsequently tested in beam in July. The results of the test-beam are presented in the next section.

4. Functional tests of the prototype in particle beams

The goal of the test-beam was to validate the mechanical design of the $1 \times 1\,\mathrm{m}^2$ prototype, to measure its response to MIPs and to test its principal functionalities. The test set-up consists of the large prototype and a telescope of small Micromegas chambers and 3 scintillating paddles of $6 \times 16\,\mathrm{cm}^2$ read out by photomultiplier tubes (PMT) (see [17] for a detailed description of the telescope). This setup-up was installed at the CERN SPS facility in the beam line H4 and exposed to 150 GeV/c muons and pions. The position of all Micromegas chambers are such that the beam trajectory is perpendicular to their pad plane. During the pion runs, a 20 cm long block of iron ($10 \times 10\,\mathrm{cm}^2$ cross-section) was placed between the telescope and the prototype to study its behaviour in hadron showers. The trigger was generated by the time coincidence of the 3 PMT signals and delayed by 1.5 μs before reaching the detectors in order to accommodate for the peaking time of the $1 \times 1\,\mathrm{m}^2$ prototype electronics. To account for the dead time of the telescope and prototype, a gate signal enters the coincidence such that any PMT signal generating during the readout of the detectors will be vetoed. The dead time of the whole set-up is dominated by the telescope and is ~ 10 ms.

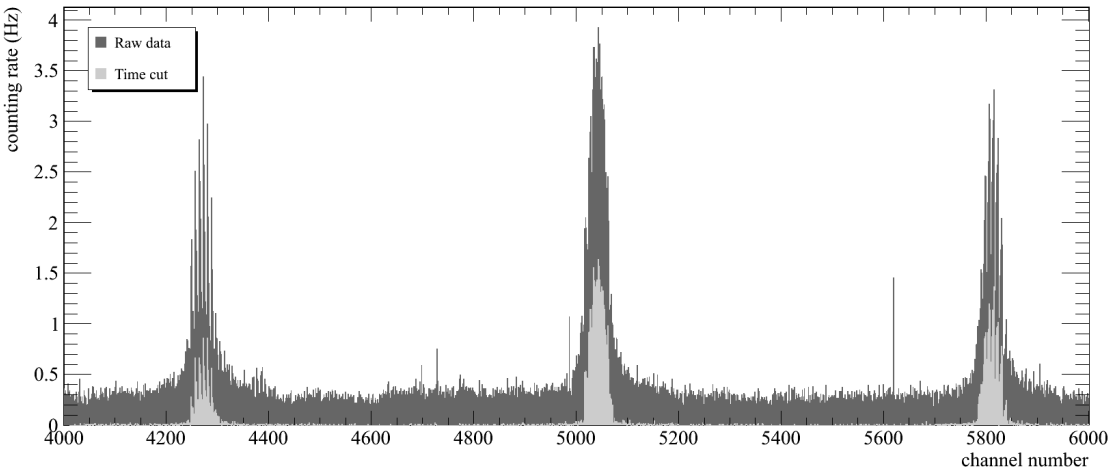

Figure 8. Channel occupancy for all hits and for hits in time with the trigger.

4.1 Noise conditions in triggered operation

The noise conditions are evaluated by identifying in the $1 \times 1\,\mathrm{m}^2$ prototype data the contributions from beam muons, cosmics particles and electronic noise. To this end, a low intensity muon beam of 250 Hz collimated to roughly the size of the scintillators ($\sim 100\,\mathrm{cm}^2$) was used. The mesh voltage was set to 370 V at which a MIP efficiency larger than 95 % is reached (cf. section 4.4). The thresholds were equalised according to the procedure previously described, resulting in a number of disabled channels of 10.

The three contributions can be seen in Figure 8 which depicts the counting rate of ~ 25 % of the prototype channels. Beam muons appear as broads peaks (the peak shapes are partly the result of the channel mapping) and a few relatively noisy channels are spotted as isolated peaks. The background from cosmic particles is essentially flat which demonstrates good noise conditions. By applying a cut on the time of the trigger ($\Delta t = 1\,\mu$s), cosmics and noise hits are fully suppressed as illustrated in Figure 8. It can be noted that this cut removes some hits from beam particles as well. These particles traverse the prototype during a readout. Although vetoed by the trigger, they can still be recorded by the prototype because its dead time is shorter than the one of the telescope and because its electronics is self-triggered.

4.2 Trigger-less operation

Thanks to the excellent noise conditions reported in the previous section, the $1 \times 1\,\mathrm{m}^2$ prototype can actually be operated without an external trigger. In this trigger-less mode, no telescope nor trigger electronics are used: the prototype is read out when a memory full signal sent by a MICROROC is received at a DIF board (in trigger mode, a memory full signal resets all chip memory and does not introduce dead time). The beam and voltage settings of the trigger mode test are used.

A simple way to verify that the prototype is efficient in this mode is to compare the average time between readouts in spill to its expected value. The latter is calculated simply as the ratio of the memory event depth (127) to the highest chip counting rate (~ 130 Hz) and is roughly 1 s.

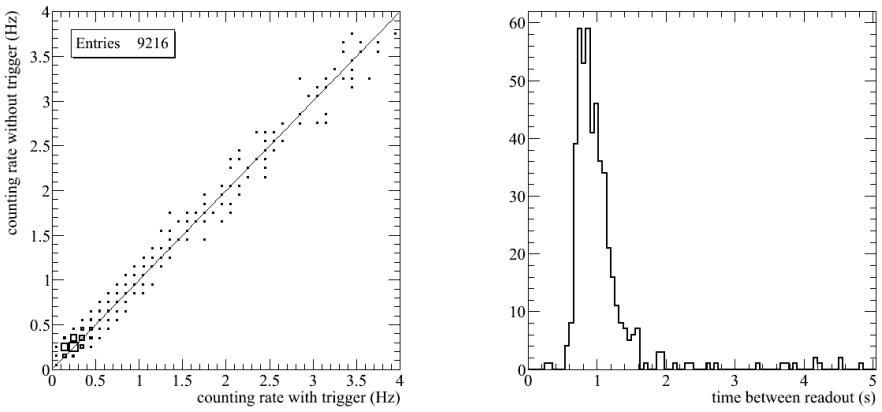

Figure 9. Time between readout in trigger-less mode (left). Channel counting rate during spills (right): trigger versus self-trigger mode.

This is in agreement with measurements as illustrated in Figure 9 (left). Another evidence for an efficient operation of the prototype in trigger-less mode is showed in Figure 9 (right) where the channel counting rates in the two modes are compared and found similar. Successful operation without trigger is possible because of the negligible noise and spark rates which are the result of a precise electronic calibration and a reliable mesh manufacturing technique.

4.3 Response of the six Micromegas meshes

The prototype was moved across the beam to measure the MIP efficiency and hit multiplicity of the 6 ASU. A muon beam of similar intensity as in the previous studies was directed at the centre of each ASU. At each position, roughly 10^5 triggers were recorded. Efficiency and hit multiplicity are deduced from the distribution of the number of hits per triggering muons. This distribution is built by finding a track in the telescope, extrapolating its impact at the prototype and counting the number of hits in time with the trigger inside a search region centred around the pad containing the extrapolated track position. Events are selected by applying the following cuts:

1. Telescope cut
   Single aligned hits in the 3 chambers to select tracks with minimum angle w.r.t. the beam axis and to extrapolate the track position at the prototype in the most precise way. This cut reduces the statistics by roughly one third.

2. Prototype cut
   No hits in time with the trigger outside the search region to reduce the impact of multiple scattering on the measured efficiency. The radial distribution of hits (in time with the trigger) w.r.t. the extrapolated pad falls rapidly and has a long tail from muons scattered in the last telescope chamber. As a result, a search region of 7×7 pads is chosen. This cut reduces further the statistics by 5 %.

About 30 thousand events pass the selection for each ASU. They are used to build the distribution of the number of hits above the 3 threshold. The efficiency ε of a given threshold is calculated as the probability to have at least one hit in the search region:

$$\varepsilon = 1 \; - \; N_0 \; / \; N_\mathrm{t} \tag{4.1}$$

and the hit multiplicity m as the average number of hits in the search region provided there is at least one hit in the search region:

$$m = \sum_{\mathrm{i}=1}^{21} \; i \; \frac{N_\mathrm{i}}{N_\mathrm{t} - N_0} \tag{4.2}$$

where N_i is the number of events with "i" hits and N_t the total number of events. Efficiency and hit multiplicity have been calculated for the 6 ASU and for the 3 thresholds. For the low threshold, high efficiency and low multiplicity are observed, with little spread from ASU to ASU (Table 2). As expected, smaller values are observed for the medium and high thresholds. Because these two thresholds are set within the signal distribution, their response is more sensitive to the detector non-uniformity than the one of the low threshold and indeed, more spread is observed. These variations could be due to small differences of the amplification gap size from one ASU to the other. They are, however, not too large and could be attenuated by adjusting the mesh voltage or the corresponding chip thresholds. In section 4.7, a way to calculate these corrections using the direct readout of shaper signals is presented.

ASU number	1	2	3	4	5	6
ε_0 (%)	97.7	97.5	98.7	98.2	98.2	96.6
m_0 (%)	1.064	1.072	1.079	1.080	1.075	1.079
ε_1 (%)	34.8	36.7	46.4	41.0	38.6	46.0
m_1 (%)	1.033	1.033	1.035	1.035	1.037	1.033
ε_2 (%)	3.7	3.7	4.6	4.0	4.0	4.6
m_2 (%)	1.050	1.057	1.059	1.075	1.052	1.046

Table 2. *MIP efficiency and hit multiplicity of the 6 ASU for the 3 thresholds.*

4.4 Effect of the peaking time

The MICROROC chip was designed for various MPGD geometries, for instance with a Bulk mesh of different gap size or even with a Gas Electron Multiplier structure. For this purpose, the peaking time of the preamplifier can be set to 75, 115, 150 or 200 ns (the latter being the default value of the $1 \times 1\,\mathrm{m}^2$ prototype). In the gas mixture used, the signal from the multiplication of a single primary electron in a 128 μm gap consists of a fast electron peak ($\sim$ 1 ns) and a long ion tail ($\sim$ 100–200 ns). For a traversing MIP, the signal is the sum of, on average, 30 primary electrons arriving at the mesh

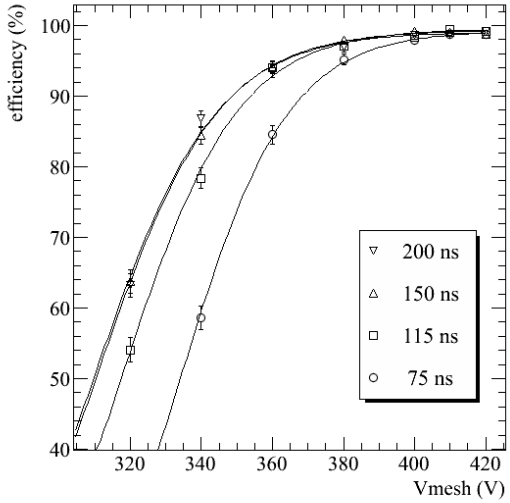

Figure 10. MIP efficiency versus mesh voltage for various peaking time of the MICROROC.

in about 30 ns. Therefore, a strong dependence of the efficiency on the peaking time is expected and has been measured.

This dependence was measured by performing a voltage scan for the 4 different values of the peaking time in a muon beam directed at the centre of one ASU. The efficiency is calculated as explained in the previous section. The 150 ns and 200 ns trends showed in Figure 10 are similar, meaning that the Micromegas MIP signal is completed in 150 ns or less. The loss of efficiency from 150 ns to 115 ns peaking time indicates, however, that the signal lasts longer than 115 ns which is compatible with expectations. At shorter peaking times, an efficiency larger than 95 % can be maintained by increasing the gas gain. This is illustrated in Table 3 where the voltages for 95 % efficiency are summarised: the loss of signal when changing the peaking time from 200 ns to 75 ns is compensated by a 20 V increase of mesh voltage. These voltages are calculated using the empirical parametrisation:

$$\varepsilon(V) = \frac{p_0}{1 + \exp\left(\frac{p_1 - V}{p_2}\right)} \tag{4.3}$$

where p_0 is the efficiency at infinite voltage, p_1 is the voltage for 50 % efficiency and p_2 describes the rise of the $\varepsilon(V)$ trend. All adjusted p_0 parameters are compatible and yield an average of 99.3 ± 0.3 %. The fact that this asymptotic value is not equal to 1 could be explained by the dead zone from the mesh supporting pillars. The voltage p_1 decreases at longer peaking time as a result of the increased available signal and becomes constant between 115–150 ns. At decreasing peaking times below 115 ns, the efficiency rises faster with voltages which is accounted for by smaller p_2 values.

4.5 Impact of dead zones between ASUs

Non-instrumented areas inside the prototype amount to 1.5 % of the total area occupied by the 6

t_p (ns)	75	115	150	200
p_0 (%)	99.3 ± 0.3	99.6 ± 0.3	99.4 ± 0.3	99.1 ± 0.3
p_1 (V)	333.9 ± 0.7	317.4 ± 0.8	310.1 ± 0.9	309.4 ± 0.8
p_2 (V)	15.2 ± 0.5	16.3 ± 0.7	17.0 ± 0.8	17.1 ± 0.7
$V(\varepsilon = 95\,\%)$ (V)	380.9	366.7	362.6	363.0

Table 3. *Parameters describing the voltage dependence of the efficiency fot various peaking time of the MICROROC. The voltage necessary to reach an efficiency of 95 % is indicated in the last line.*

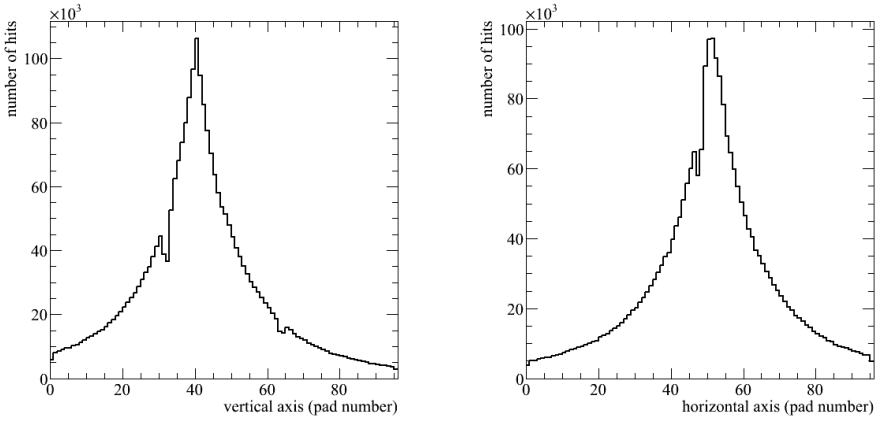

Figure 11. Vertical and horizontal profiles of pion showers ($\sim 5{\cdot}10^4$ triggers).

ASUs ($96.5 \times 97\,\mathrm{cm}^2$). Another contribution to the prototype inefficiency may come from possible non-uniformity of the electric field at the ASU edges. This hypothesis was tested by placing a block of iron along a pion beam (collimated to a $3 \times 3\,\mathrm{cm}^2$ region) and measuring downstream of the block secondary particles produced in hadron showers. In this way a large fraction of the prototype is exposed and possible discontinuities in the measured hit profile can be looked for. For this measurement, the mesh voltages were set to 375 V.

Considering the block size ($10 \times 10\,\mathrm{cm}^2$ transverse size and 20 cm length along the beam), roughly half of the pions experience a nuclear interaction inside the block. The distribution of the number of hits in the prototype thus shows a peak at 1 hit from penetrating pions and a long tail up to 300 hits from showering pions. Horizontal and vertical profiles of showers only are constructed by rejecting events with a hit multiplicity below 3. They are showed in Figure 11 where a small drop of efficiency for pads at the ASU edges is observed. By extrapolation of the inner pad occupancy to the ASU edges, the number of hits is 20 % lower than what it should be. The number of pads at the ASU edges is 576 (out of 9216 which yields a fraction of 6.2 %). This can be interpreted as a dead zone of 1.25 % which adds to the 1.5 % from non-instrumented areas, leading to less than 3 % of the prototype being inefficient.

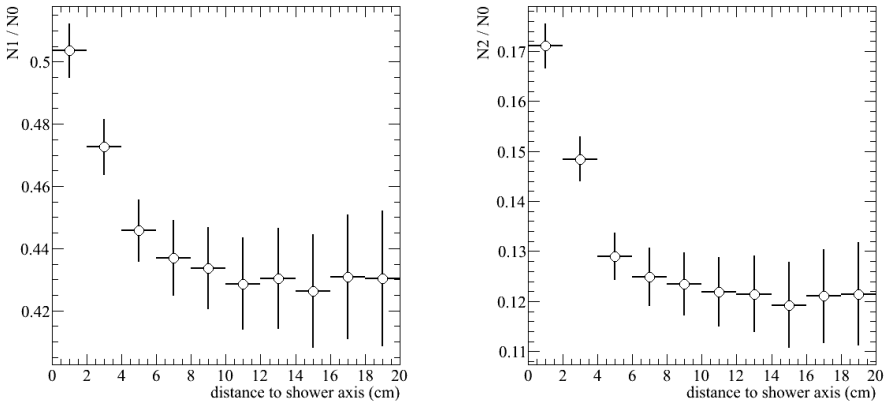

Figure 12. Medium and high threshold efficiency in hadron showers versus distance to the shower axis.

4.6 Shower sampling with three readout thresholds

Hadron showers develop on average into a dense electromagnetic core from neutral meson decays surrounded by a halo of particles (muons, charged pions, protons etc...). Saturation in a DHCAL will be caused mainly by the electromagnetic part and additional thresholds are introduced to perhaps mitigate this effect by identification and weighting of low, medium and high energy deposits. This identification capability can be illustrated by measuring the threshold efficiencies for various energy deposits. Because the energy density decreases with the distance to the shower axis, the efficiencies were measured as a function of position using the setup-up described in the previous section. The mesh voltage was 370 V and the thresholds were set at rougly (2 fC, 2 MIP, 10 MIP).

Because the MIP efficiency of the low threshold is high ($\leq 95\,\%$), the efficiency of the other thresholds can be approximated to N_1 / N_0 and N_2 / N_0 where N_k is the number of hits from threshold "k". These ratios are plotted versus distance to the shower axis in Figure 12. Both trends indicate that the electromagnetic core is contained in a circle of 10 cm radius. Compared to the halo, the core has a higher energy density which explains the probability variation with distance: N_1 / N_0 increases from 0.43 to 0.51 and N_2 / N_0 from 0.12 to 0.17. This measurement illustrates the possibility to identify the electromagnetic part of hadron showers which is a necessary condition for offline compensation of a Micromegas semi-digital hadron calorimeter.

4.7 Analogue readout of shaper signals

A correction of the mesh voltage or of the readout threshold may be necessary to improve the response uniformity of the prototype, in particular for the medium and high thresholds (cf. section 4.3). The most straight-forward way to calculate the correction is to have access directly to the signal distribution. For this reason, dedicated lines were implemented on the ASU to read out the output voltage of the low gain shaper. The analogue readout uses a trigger signal that first arrives at the DIF. After a certain programmable delay to match the peaking time of the MICROROC, the DIF forwards the signal at the chips. The voltages of the shaper outputs of all channels are then multiplexed and sent to the DIF where they are digitised with a 12-bit resolution.

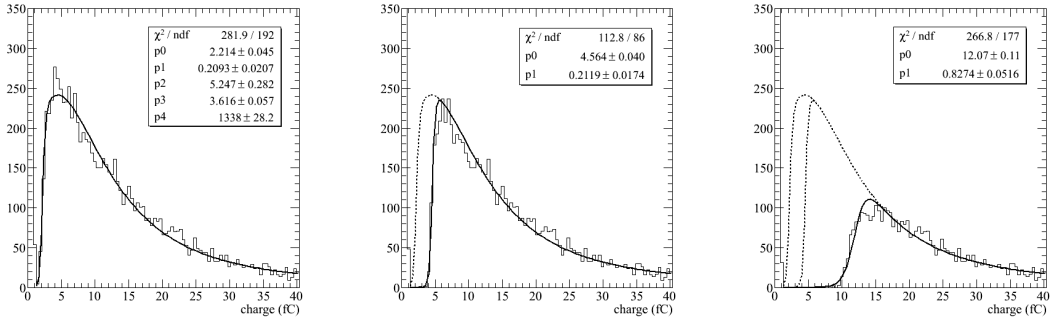

Figure 13. Muon Landau distribution from low, medium and high threshold hits.

The analogue readout was tested in a beam of muons. The Landau distribution as measured on roughly 100 pads and corrected for channel to channel pedestal variations is shown in Figure 13 (left). By applying cuts on low, medium or high thresholds, the signal distribution is cropped from 0 to the threshold value which can thus be measured in unit of charge (Figure 13 (left to right)). More importantly, it is also possible to measure the thresholds in unit of the MIP value which is the natural energy unit in a calorimeter. For instance, threshold and MIP values can be extracted from the data using the following parametrisation of the charge spectrum:

$$f(q) = s(q, p_0, p_1) \cdot l(q, p_2, p_3, p_4) \tag{4.4}$$

where $s(q)$ is a sigmoid function of inflexion point p_0, width p_1 and with a maximum value of 1 that accounts for the channel to channel threshold dispersion. The function $l(q)$ is the Landau function of most probable value p_3, width p_4 and normalisation factor p_2. When adjusting the parameters to the data of Figure 13, it is found that (for this particular run) low, medium and high thresholds are respectively equal to 0.6, 1.3 and 3.3 times the MIP value.

4.8 Power-pulsing of the front-end chips

The circuits of a MICROROC chip can be turned on and off rapidly according to an external digital signal (*e.g.* the accelerator clock). When the chip is turned on, a certain programmable delay is applied before any detector signal can be recorded to the memory. This delay accounts for the stabilisation of the various voltages and currents inside the chip and should be minimum to reduce the power consumption. If the delay is too short, the detector occupancy is dominated by noise until stabilisation. This is illustrated in Figure 14 (left) where the number of hits in the $1 \times 1\,\mathrm{m}^2$ prototype is plotted versus time for a short run in trigger-less mode. During the run, a power-pulsing timing of 4.5 s off and 3 s on was used and the delay was set to 50 μs. When using a delay of 100 μs (Figure 14 (right)), the high peaks every 7.5 s disappear because stabilisation has been achieved. For a bias voltage of 5 V, the current drops from 11 A to 3 A when the chips are turned off. The 3 A correspond to the consumption of the 3 DIF and inter-DIF boards of the prototype.

5. Conclusion

A Micromegas prototype of $1 \times 1\,\mathrm{m}^2$ consisting of six independent Micromegas boards with inte-

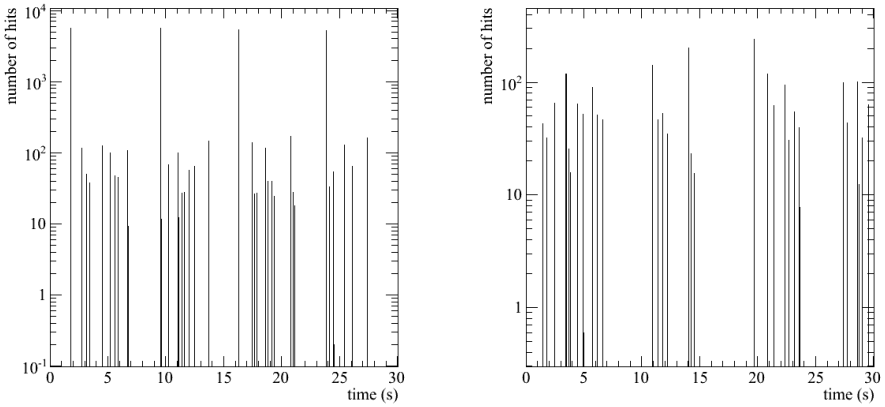

Figure 14. Number of hits versus time using power-pulsing of the chips with 50 μs (left) and 100 μs (right) delay between the power signal and the start of the trigger-less acquisition.

grated 2-bit front-end electronics has been constructed. This modular design, although introducing little dead zones (below 3 %), allows to achieve an overall thickness of 9 mm and a uniform drift gap over the prototype area. Thanks to adequate discharge protections and low noise front-end circuits, more than 99.98 % of the 9216 prototype channels are operational. Most importantly, the six Micromegas boards exhibit comparable performance to ionising radiations and all provide the necessary gas gain for a 98 % efficiency to minimum ionising particles.

Compared to a pure digital gaseous calorimetry, an approach with three thresholds will rely strongly on the proportionality of the sampling detector and on its cell to cell signal uniformity. This kind of Micromegas is free of saturation effects and its amplification gap is precisely defined by the mesh supporting pillars over the anode plane. Variations of this gap have probably been observed from mesh to mesh. Based on the direct readout of detector signals, however, a technique to correct the mesh voltage of chip thresholds is possible. Combined with other features such as power-pulsing and self-triggering, the constructed Micromegas prototype is therefore a good candidate for Particle Flow calorimetry at a future linear collider.

References

[1] A. Djouadi et al., *International Linear Collider Reference Design Report Volume 2: PHYSICS AT THE ILC*, *arXiv:hep-ph* **0709.1893** (2007).

[2] CLIC Physics Working Group, *Physics at the CLIC Multi-TeV Linear Collider*, *arXiv:hep-ph* **0412251** (2004).

[3] ATLAS collaboration, *Observation of a new particle in the search for the Standard Model Higgs boson with the ATLAS detector at the LHC*, *Physics Letters B* **716** (2012) 1.

[4] CMS collaboration, *Observation of a new boson at a mass of 125 GeV with the CMS experiment at the LHC*, *Physics Letters B* **716** (2012) 30.

[5] *The RD52 experiment, http://highenergy.phys.ttu.edu/dream.*.

[6] *The CALICE collaboration, https://twiki.cern.ch/twiki/bin/view/CALICE.*

[7] R. Wigmans, *The DREAM project-Results and plans*, *Nucl. Instr. and Meth. A* **572** (2007) 215.

[8] J.-C. Brient, H. Videau, *The calorimetry at a future e^+e^- linear collider*, *arXiv:hep-ex* **0202004v1** (2002).

[9] M.A. Thomson, *Particle flow calorimetry and the PandoraPFA algorithm*, *Nucl. Instr. and Meth. A* **611** (2009) 25.

[10] V. Andreev et al., *A high-granularity scintillator calorimeter readout with silicon photomultipliers*, *Nucl. Instr. and Meth. A* **540** (2005) 368.

[11] B. Bilki et al., *Calibration of a digital hadron calorimeter with muons*, *JINST* **3** (2008) 05001.

[12] S. Mannai et al., *High granularity Semi-Digital Hadronic Calorimeter using GRPCs*, *Nucl. Instr. and Meth. A, Article in Press* (2012).

[13] A. Ghezzi, T. Tabarelli de Fatis, G. Tinti, *Digital Hadron Calorimetry with Glass RPC Active Detectors*, *arXiv:physics* **0507021** (2005).

[14] C. Adloff et al., *Monte Carlo study of the physics performance of a digital hadronic calorimeter*, *JINST* **4** (2009) 11009.

[15] *SiD Letter of Intent*, *arXiv/physics.ins-det* **0911.0006** (2009).

[16] Y. Giomataris et al., *MICROMEGAS: a high-granularity position-sensitive gaseous detector for high particle-flux environments*, *Nucl. Instr. and Meth. A* **376** (1996) 29.

[17] C. Adloff et al., *MICROMEGAS chambers for hadronic calorimetry at a future linear collider*, *JINST* **4** (2009) 11023.

[18] I. Giomataris et al., *Micromegas in a bulk*, *Nucl. Instr. and Meth. A* **vol** (year) page.

[19] C. Adloff et al., *MICROROC: MICRO-mesh gaseous structure Read-Out Chip*, *JINST* **7** (2012) 01029.

[20] *Omega, microelectronics for physics and medical imaging: http://omega.in2p3.fr/.*

[21] M. Chefdeville, *Development of Micromegas-like gaseous detectors using a pixel readout chip as collecting anode*, *CERN Document Server* **PhD Thesis** (2009) 151.

[22] S.F. Biagi, *Monte Carlo simulation of electron drift and diffusion in counting gases under the influence of electric and magnetic fields*, *Nucl. Instr. and Meth. A* **421** (1999) 234.

[23] F. Sauli, *Principles of operation of Multiwire Proportional and Drift Chambers*, *CERN Yellow Reports* **77-09** (1977).

[24] J. Bouchez et al., *Bulk micromegas detectors for large TPC applications*, *Nucl. Instr. and Meth. A* **547** (2007) 425.